AGU100 ADVANCING EARTH AND SPACE SCIENCE

JGR

Journal of Geophysical Research: Planets

RESEARCH ARTICLE

10.1029/2018JE005717

†These authors are visiting astronomers from the National Solar Observatory, operated by the Association of Universities for Research in Astronomy, Inc. (AURA), under cooperative agreement with the National Science Foundation.

Key Points:

- Comprehensive sets of direct lunar exospheric line width observations are presented as a function of lunar phase
- Exospheric temperatures are highest near full Moon and decrease toward large phase angles
- Photon stimulated desorption dominates source mechanisms at subsolar points, with contributions by other processes near terminators

Supporting Information:

- Supporting Information S1
- Table S1

Correspondence to:
D. C. P. Kuruppuaratchi,
kuruppud@my.erau.edu

Citation:
Kuruppuaratchi, D. C. P., Mierkiewicz, E. J., Oliversen, R. J., Sarantos, M., Derr, N. J., Gallant, M. A., et al. (2018). High-resolution, ground-based observations of the lunar sodium exosphere during the Lunar Atmosphere and Dust Environment Explorer (LADEE) mission. *Journal of Geophysical Research: Planets*, *123*, 2430–2444. https://doi.org/10.1029/2018JE005717

Received 11 JUN 2018
Accepted 13 AUG 2018
Accepted article online 25 AUG 2018
Published online 23 SEP 2018

High-Resolution, Ground-Based Observations of the Lunar Sodium Exosphere During the Lunar Atmosphere and Dust Environment Explorer (LADEE) Mission

D. C. P. Kuruppuaratchi[1], E. J. Mierkiewicz[1†], R. J. Oliversen[2†], M. Sarantos[2], N. J. Derr[3,4†], M. A. Gallant[1†], S. A. Rosborough[1†], C. W. Freer[1†], L. C. Spalsbury[5†], D. D. Gardner[3,6†], O. L. Lupie[2†], and F. L. Roesler[3]

[1]Department of Physical Sciences, Embry-Riddle Aeronautical University, Daytona Beach, FL, USA, [2]NASA Goddard Space Flight Center, Greenbelt, MD, USA, [3]Department of Physics, University of Wisconsin-Madison, Madison, WI, USA, [4]School of Engineering and Applied Sciences, Harvard University, Boston, MA, USA, [5]Adnet Systems Inc., Greenbelt, MD, USA, [6]Department of Planetary Sciences, University of Arizona, Tucson, AZ, USA

Abstract We present the first comprehensive set of lunar exospheric line width and line width derived effective temperatures as a function of lunar phase (66° waxing phase to 79° waning phase). Data were collected between November 2013 and May 2014 during six observing runs at the National Solar Observatory McMath-Pierce Solar Telescope by applying high-resolution Fabry-Perot spectroscopy ($R \sim 180{,}000$) to observe emission from exospheric sodium (5,889.9509 Å, D2 line). The 3-arc min field of view of the instrument, corresponding to ~336 km at the mean lunar distance (384,400 km), was positioned at several locations off the lunar limb; only equatorial observations taken out to 950 km are presented here. We find the sodium effective temperature distribution to be approximately a symmetric function of lunar phase with respect to full Moon. Within magnetotail passage we find temperatures in the range of 2500–9000 K. For phase angles greater than 40° we find that temperatures flatten out to ~1700 K.

Plain Language Summary High spectral resolution observations of optical line emissions are used to investigate the morphology and dynamics of the lunar sodium exosphere. These observations were obtained from the National Solar Observatory McMath-Pierce Solar Telescope, coincident with the Lunar Atmosphere and Dust Environment Explorer mission. The equatorial data presented here are the first comprehensive set of direct sodium emission line profile observations of the lunar exosphere. These observations will help constrain atmospheric and surface process modeling, and help quantify lunar exospheric source and escape mechanisms. Studying the morphology of the lunar exosphere with altitude and local time provides a useful *laboratory* for testing space weather effects at Earth and theoretical models of other bodies with similar exospheres (e.g., Mercury).

1. Introduction

The lunar atmosphere, commonly referred to as a surface-bounded exosphere, is collisionless and tenuous in nature and is constantly being replenished and lost (Stern, 1999) with sodium being one of the easiest constituents to observe. Source mechanisms that maintain the Moon's exosphere include thermal desorption, photon-stimulated desorption (PSD), charged particle sputtering, impact vaporization, and outgassing of species through radioactive decay (i.e., argon). The first three processes result in a sodium distribution that is expected to vary with solar zenith angle (SZA; with a maximum at the subsolar point), whereas impact vaporization by a sporadic meteoroid source produces a density distribution that is not spherically symmetric around the Moon, exhibiting a strong enhancement near the morning terminator (Horányi et al., 2015; Janches et al., 2018). The relative importance of each of these sources of exospheric sodium remains somewhat uncertain, both regarding their spatial (e.g., due to variations in the lunar surface composition) and temporal (e.g., the 29.5-day lunar diurnal cycle) influences (Morgan & Shemansky, 1991; Potter et al., 2000; Sarantos et al., 2010; Smyth & Marconi, 1995; Sprague et al., 1992; Stern, 1999; Yokota et al., 2014). For example, while there was a strong enhancement in the lunar exosphere following the Geminids shower (Colaprete et al., 2016), no strong correlation was noted between sporadic meteoritic influx measurements made by the Lunar Dust Experiment on the Lunar Atmosphere and Dust Environment

10.1029/2018JE005717

Explorer (LADEE) and neutral exospheric density as measured by LADEE Ultraviolet-Visible Spectrometer (UVS; Szalay et al., 2016). Once released, gases in the lunar atmosphere can be pulled back to the regolith by gravity, directly escape to space, get pushed away by solar radiation pressure, or become photoionized and lost to the solar wind (Yakshinskiy & Madey, 1999).

The temperature of the lunar sodium exosphere can be attributed to a combination of collisionless nonthermal sources such as PSD and sputtering and thermal sources such as impact vaporization (Domingue et al., 2007). As such, the effective temperature (derived from the Doppler line width) of the exosphere and its altitude variation can be used as a first indicator of source processes. Although intensity distributions of the lunar sodium exosphere have been measured on several occasions (e.g., Mendillo et al., 1993; Potter & Morgan, 1988a, 1988b; Tyler et al., 1988), exospheric temperatures have mainly been inferred from model fits to the observed distributions with altitude (e.g., Kagitani et al., 2010; Potter et al., 2000; Sprague et al., 1992, 2012). One exception is the direct line width observations of Mierkiewicz et al. (2014), which we extend in this work. Line width measurements differ from the observed altitude (scale height) distributions by offering a direct probe of the tangential kinematics (velocities) of the observed exospheric column.

Observed altitude distributions of sodium imply two populations consisting of *hot* (i.e., suprathermal) and *cold* sodium atoms. The hot component is presumed to be a population of recently released sodium atoms from meteoroid impacts, photosputtering, and/or solar wind sputtering; the cooler population is a result of thermal desorption and/or collisional thermalization of the primary (hot) population via interactions with the lunar surface (Ip, 1991; Morgan & Shemansky, 1991; Potter & Morgan, 1988b, 1991; Sprague et al., 1992; Stern, 1999). The direct line width measurements of Mierkiewicz et al. (2014) indicated that sodium temperatures are highest near full Moon and decrease toward large phases—a result similar to scale height derived temperatures by Potter et al. (2000). Mierkiewicz et al. (2014) attributed their observed line width derived temperatures to an energetic nonthermal (suprathermal) process, consistent with conclusions reached by altitude distribution observations (e.g., Potter et al., 2000; Sprague et al., 1992).

A second indicator of the source nature is the dependence of the exospheric column with angle from the subsolar point. Imaging (Mendillo et al., 1993; Potter & Morgan, 1998) and spectroscopic (Sprague et al., 1992, 2012) observations indicate that the distribution of atmospheric sodium along the limb visible from Earth appears to peak at the subsolar point. Furthermore, the variation in the emission changes more rapidly with SZA than a cosine function (i.e., than a pure photodesorption source) and falls off as $\cos^k$ (SZA) where $k \geq 2$ (e.g., Mendillo et al., 1997; Potter & Morgan, 1998). Sprague et al. (1992) suggested that thermal desorption dominates near the subsolar point and photodesorption dominates at high SZAs. Note that thermal desorption of alkalis is only possible close to the subsolar point since it is temperature dependent and is also expected to be less efficient on the Moon compared to Mercury (Madey et al., 1998).

Based on evidence provided by the temperature and altitude distribution of sodium, previous studies (e.g., Madey et al., 1998; Sarantos et al., 2010; Sprague et al., 1992; Tenishev et al., 2013; Yakshinskiy & Madey, et al., 1999) argued that PSD is the major source mechanism for the lunar sodium exosphere. It was furthermore proposed that PSD varies both temporally and spatially due to the variability of the ion influx to the surface. As the Moon moves from a pure solar wind environment and spends approximately 6 days per month within the Earth's magnetosphere, it is bombarded by ions of variable energies and fluxes (Mendillo et al., 1997; Sarantos et al., 2008, 2010). Potter and Morgan (1994) and Potter et al. (2000) observations before, during, and after lunar passage through the Earth's magnetotail indicated that impacts by the solar wind may be a significant source of sodium in the lunar atmosphere. Wilson et al. (2006) demonstrated that the difference in sodium brightness observed in five separate eclipses was correlated to the augmentation of the lunar sodium exosphere through ion sputtering when the Moon moved from residing in the cooler plasma in the lobes to the hotter denser plasma in the plasma sheet. This suggests that the type of plasma environment the Moon interacts with (solar wind, magnetotail lobes, magnetosheath, and plasma sheet) influences the lunar sodium exosphere. Potter et al. (2000) and Sarantos et al. (2010) suggested that solar wind ions and the energetic particles found in the plasma sheet cause *priming* of the lunar surface (e.g., via ion-enhanced diffusion), which allows PSD to release sodium atoms from the surface more efficiently. Modeling by Sarantos et al. (2010) had to assume that the PSD efficiency is variable over a month (e.g., higher when the Moon is exposed to the solar wind) to explain the rate of brightening of the lunar exosphere from full to quarter Moon as seen by an Earth observer. Sprague et al. (2012) used a comprehensive summary of all available observations to date to find that the lunar sodium was statistically brighter when exiting full Moon phase than entering it, similar to the continuous sequence of observations of Potter et al. (2000), a result which was interpreted to mean that Earth's plasma sheet ions effectively enrich the sodium reservoir.

In addition to the possible effects of PSD efficiency by a variable ion influx rate, another driving mechanism that may influence the lunar exosphere is impacts by meteor sources (sporadic and showers). Previous ground-based studies have explored the possible effects of micrometeoroid impact vaporization on the lunar exosphere and observed an increase in exospheric sodium abundances through the Leonids (Smith et al., 1999) and the Taurids (Verani et al., 1998). These observations, along with space-based observations (Colaprete et al., 2016; Szalay et al., 2016), showed that micrometeoroid bombardment is not a dominant source mechanism of the exosphere but is sporadic in nature.

Two robotic missions have made space-based observations of the lunar sodium exosphere over a continuous period. The first of these observations was made by the Kaguya spacecraft's Telescope for Visible Light (TVIS) instrument (December 2008 to June 2009; Kagitani et al., 2010). The second of these observations was made by LADEE UVS (November 2013 to April 2014; Colaprete et al., 2016). In addition to UVS, LADEE also measured lunar exospheric ions including Na^+ from the Neutral Mass Spectrometer instrument (Halekas et al., 2015). Kaguya TVIS observations from the lunar nightside suggested a spherically symmetric distribution of the sodium exosphere with a temperature range of 2400–6000 K (Kagitani et al., 2010). Furthermore, Kagitani et al. (2010) inferred from observations during two lunar cycles that the sodium density gradually decreased from first to third quarter by about 20 ± 8%. LADEE UVS observations of the dayside showed that as the Moon made its passage into Earth's magnetotail, the total sodium abundance first decreased then increased through full Moon until a maximum value at ~ 30° phase angle was reached, contrary to the ongoing decrease in sodium abundances that was seen by Kaguya TVIS. LADEE UVS also clearly demonstrated the importance of micrometeoroid bombardment for supplying the lunar exosphere during showers such as the Geminids and suggested a possible correlation between sodium and surface albedo (Colaprete et al., 2016), which is perhaps a manifestation of large sodium enhancements on the nearside lunar surface revealed by the Chandrayaan-1 X-ray Spectrometer (Athiray et al., 2014).

In summary, much remains to be understood about the processes that populate the lunar sodium exosphere despite the availability of 30 years of observations. Here we present the first comprehensive set of line width and line width derived effective temperatures from a series of ground-based observing runs conducted between November 2013 and May 2014 at the National Solar Observatory McMath-Pierce Solar Telescope at Kitt Peak. Line profile measurements provide additional constraints to models of the physical processes, such as clues to the bulk motion of the gas. Data presented here include phase angle coverage from 66° waxing phase to 79° waning phase. Our observation and data analysis strategy is described in section 2 followed by our line width, line width derived temperature, relative intensity, and Doppler velocity results in section 3. We analyze our results and put them in the context of previous ground-based observations, solar cycle variation, and modeling efforts in section 4, followed by a summary and conclusions in section 5.

2. Observations and Data Analysis

We employ high-resolution (R ~ 180,000) Fabry-Perot line profile observations to investigate the morphology and dynamics of the lunar sodium atmosphere. Observations were carried out by a Fabry-Perot Spectrometer (FPS), as described in Mierkiewicz et al. (2014). The data were collected in the annular summing mode which allowed the entire 0.08-nm spectral range of interest to be simultaneously imaged onto a charge-coupled device detector in one exposure (Coakley et al., 1996). Observations were made over six runs from November 2013 to May 2014 and were concurrent with the LADEE mission's testing and science phase.

The observing sequence was as follows. The telescope was centered on one of six selected craters (Figure 1) and then moved in right ascension (a) or declination (δ) to the lunar limb. Data were collected with the FPS's 3-arc min field of view (FOV; corresponding to ~336 km at the mean lunar distance of 384,400 km) tangent to the limb and then in a series of defined offsets out to two lunar radii. Only east and west equatorial data off the sunlit limb are presented here, starting from a FOV-centered 1.5 arc min, 4.9 * cos(δ) arc min, and 8.5 * cos(δ) arc min off the limb; where δ is the declination of the Moon (refer to Figure 2 in Mierkiewicz et al., 2014). For the mean lunar distance, these offsets correspond to 168 km, 550 * cos(δ) km, and 950 * cos(δ) km, respectively. Observations were also made on the lunar central highlands (near Moon center) and 40 arc min

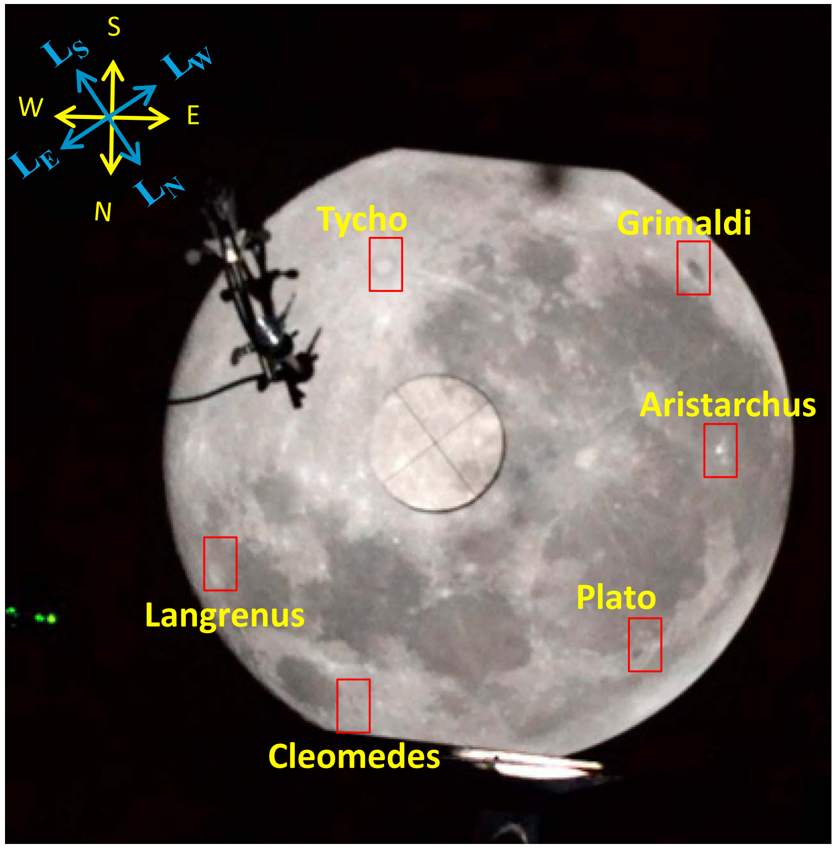

Figure 1. Image of the Moon at the focal plane of our instrument, with the instrument's 76-mm input aperture covered at the location of the cross hairs. The calibration lamp assembly is seen at the upper left. The telescope pointing directions are depicted by yellow arrows. Selenographic coordinates are depicted by the blue arrows where the east and west directions are laterally reversed. Both coordinate systems rotate in the telescope's focal plane as a function of hour angle (HA).

east (or west) of Moon center for intensity and sky background measurements, respectively. Moon center observations were used to assess photometric conditions. The atmospheric transparency is assumed to be similar for purposes of this relative intensity comparison. Consistent with Mierkiewicz et al. (2014), sky background measurements indicate that the terrestrial sodium emissions are negligible for observations taken within one lunar radii of the limb. All observations were obtained with the telescope tracking at the lunar rate. Observing runs were typically 7–13 days and included full Moon. April 2014 observations surrounded a lunar eclipse, but these eclipse results are not included here. Refer to Figure 1 for centering/offset craters and Table 1 for a summary of observations.

Sample Fabry-Perot sodium ring images and their corresponding spectra taken at the lunar limb offset from the Grimaldi crater and the Aristarchus crater are shown in Figures 2a and 2b, respectively. All lunar spectra were fit with a model consisting of six components and a sloping background convolved with an empirically determined instrumental function using the least squares fitting code of R.C. Woodward (private communication, June 2014); examples of the spectra, fit, and residuals are included in Figures 2a and 2b. The six-component model includes two Gaussians for the lunar sodium D2 s-resolved hyperfine structure emission components at 5889.9386 and 5889.9584 Å, a single Gaussian to fit the solar Fraunhofer absorption line at 5890.9509 Å, and three Gaussian fits to nearby terrestrial water absorption lines at 5890.227, 5890.090, and 5889.637 Å (McNutt & Mack, 1963). The widths and areas of the Gaussians representing the terrestrial water lines at 5890.227 and 5890.090 Å are linked to the stronger water feature at 5889.637 Å in a 1:1 ratio and 0.67:1 ratio, respectively.

Table 1
Summary of Data Runs

Month	Year	Run[a]	Nights with data	Full Moon date
November	2013	11/16–11/22	3	17 November
December	2013	12/13–12/20	6	17 December
January	2014	01/10–01/21	11	16 January
February	2014	02/11–02/22	8	14 February
April	2014	04/14–04/22	7	15 April
May	2014	05/09–05/20	10	14 May

[a]Run dates are formatted as MM/DD.

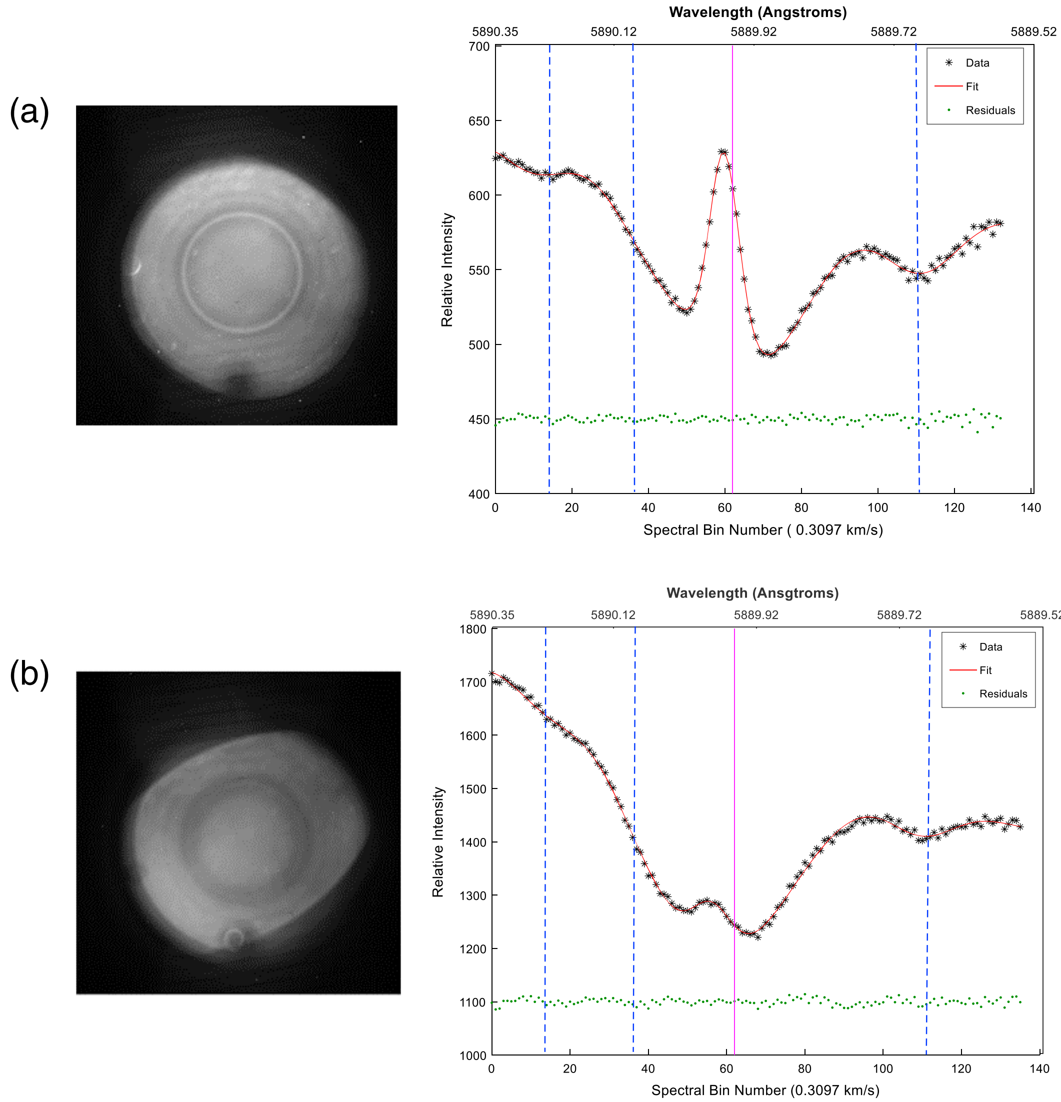

Figure 2. (a, left) Lunar sodium raw ring image and (a, right) its corresponding spectrum for an image taken on 19 February 2014, 8:37 UT at the limb off Grimaldi crater (49.85° waning phase) and (b, left) lunar sodium raw ring image and (b, right) its corresponding spectrum for an image taken on 14 February 2014, 9:06 UT off the limb off Aristarchus crater (8.72° waxing phase). Besides the reflected solar spectra, terrestrial absorption lines, and the lunar emission, the ring images include the black artifact (bottom) which is a chip in the number 2 mirror, smudges, dirt/glint from the #1 and #2 mirrors, cosmic ray hits, low contrast straight fringes toward the bottom of the ring image caused by reflections between the Fabry-Perot etalons, and scattered moonlight which causes the ring image to look asymmetric. As the field of view is off the lunar limb, the continuum is due to scattered moonlight within the Earth's atmosphere and off the telescope mirrors and superstructure. The retrieved sodium spectrum consists of a solar Na Fraunhofer absorption feature (5889.9509 Å), three terrestrial water absorption features (marked by the blue lines at 5,890.227, 5,890.090, and 5,889.637 Å), the lunar hyperfine s-resolved sodium emission doublet (5,889.9386 and 5, 889.9584 Å; rest wavelength of sodium (terrestrial frame of reference) marked by pink line) in a 3:5 intensity ratio, the model fit, and the fit residuals. Note that fit residuals have an offset of 1,100 and an offset of 450 for Figures 2a and 2b, respectively.

The widths of the Gaussians representing the two sodium emissions components at 5889.9386 and 5889.9584 Å are linked in a 1:1 ratio, while their intensities are set in a 3:5 ratio. The spectrum in Figure 2a was taken at phase angle 49.8° when the sodium emission is clearly visible due to the lower continuum level. Figure 2b was taken close to full Moon and shows a raised continuum level with less prominent terrestrial water features and sodium emission. However, we do not see any systematic pattern in our residuals and are confident with our fitting methodology.

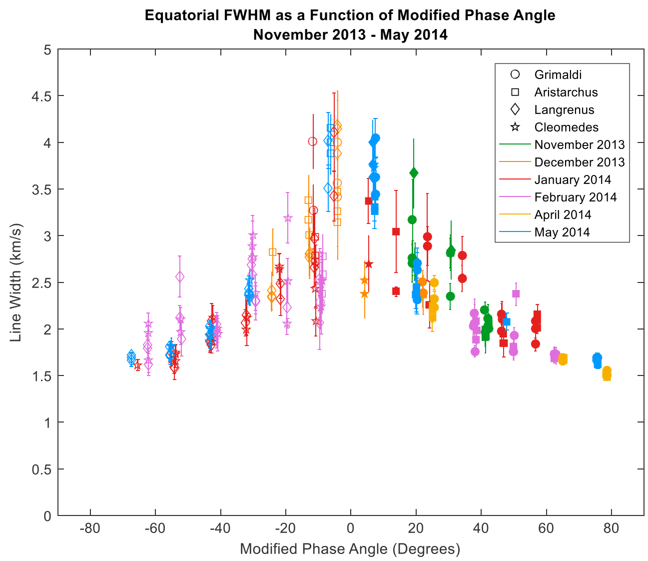

Figure 3. Line width as a function of modified phase angle for equatorial latitude regions. The modified phase angle represents waxing phase data (open symbols) as negative and waning phase data (filled symbols) as positive. Pre– and post–full Moon line widths are nearly symmetric about a phase angle of 0°, with the largest line widths occurring near full Moon. FWHM = full width at half maximum.

The observed depth of the solar Fraunhofer D2 line is significantly filled in by scattered light to approximately 70% of continuum compared to a known depth of 5% of the continuum at line center; another much smaller contribution (~1–2%) is the filling of the Fraunhofer line due to Brillouin scattering (Potter et al., 1984). Thorium calibration lines were taken nightly to monitor both wavelength and instrumental stability. Instrumental profile (IP) studies indicate an average full width at half maximum of 1.7 km/s, consistent with the earlier work of Mierkiewicz et al. (2014). For these observations, we are able to deconvolve sodium line widths to approximately one half of the IP full width at half maximum. For an explanation on how Doppler line width can be related to effective temperature, refer to Mierkiewicz et al. (2014).

3. Results

Lunar sodium line width and line width derived effective temperatures are displayed as a function of phase angle for equatorial regions in Figures 3 and 4, respectively. Locations of craters used as an offset are shown in Figure 1. To denote phase angles before full Moon, we define a modified phase angle where negative angles represent waxing phase (unfilled symbols) and positive phase angles represent waning phase (filled symbols). Line widths are similar during waxing and waning phase, with the largest line widths (effective temperatures) occurring near full Moon. A smoothing spline (piecewise polynomial) has been included in Figure 4 to highlight the systematic trend of increasing temperatures toward full Moon.

In terms of effective temperature, the exosphere is *hottest* when the Moon is inside the Earth's magnetotail; typically, for phase angles <30° (approximately 6 days), the temperature range was 2500–9000 K, with an average temperature of 4330 ± 680 K. Away from magnetotail passage, data taken at phase angles greater than 40° on the waxing side have an average temperature of 1770 ± 190 K, and for data taken at phase angles greater than 40° on the waning side the average temperature is 1700 ± 140 K. Refer to Table 2 for a list of average temperatures.

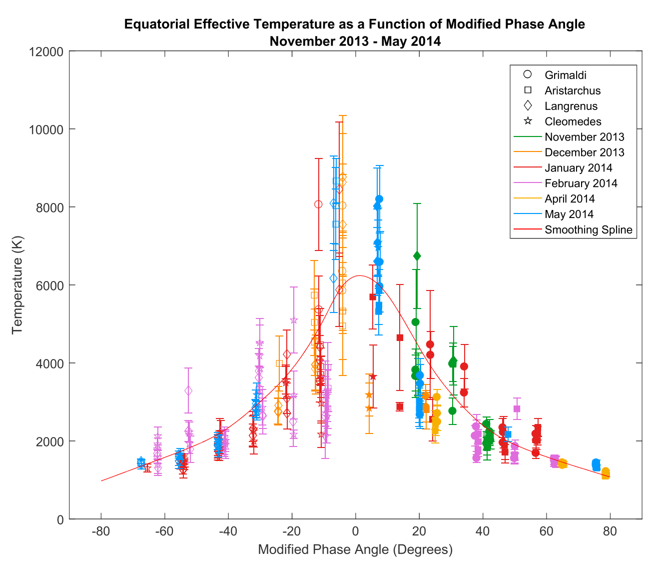

Figure 4. Temperature as a function of modified phase angle for equatorial latitude regions. Pre– and post–full Moon line widths are nearly symmetric about a phase angle of 0°, with the largest line width derived effective temperatures occurring near full Moon at the time when the Moon's orbit takes it through the Earth's magnetotail. A smoothing spline has been added to highlight the main trend of the data set.

Figure 5 compares the range of temperatures derived from our equatorial data (including uncertainties) plotted in gray along with the smoothing spline, to the scale height derived temperature data compiled by Sarantos et al. (2010), the line width derived temperature data of Mierkiewicz et al. (2014), and the scale height derived temperature data of Sprague et al. (2012). Overall, the upper range of the line width derived temperatures at small phase angles are higher than those of Mierkiewicz et al. (2014) as well as the scale height derived temperatures (e.g., by about a factor of 2–3 during magnetotail passages). The waxing and waning phase scale height derived temperatures of Potter et al. (2000) and the waning phase line width derived temperatures of Mierkiewicz et al. (2014) agree with the lower range of our data set. Note that the trend of increasing temperatures toward full Moon (small phase angles) is seen clearly in the data from Potter et al. (2000) and Mierkiewicz et al. (2014) but to a lesser extent in data from Sprague et al. (2012).

To explore the cause of the difference between data sets, all data in Figure 5 were plotted alongside the solar $F_{10.7}$ flux to indicate where in the solar cycle each data set was collected (see Figure 6a). $F_{10.7}$ data were obtained from the OMNI database (https://omniweb.gsfc.nasa.gov) and the Natural Resources of Canada database (http://www.spaceweather.gc.ca). Figure 6b shows the detrended temperature data presented here along with $F_{10.7}$ flux. We do not find a correlation with temperature and $F_{10.7}$ flux.

Table 2
Equatorial Region Line Width Derived Effective Temperatures Averaged According to the Moon's Approximate Location Relative to the Earth's Magnetotail

Limb	Modified phase angle < −40° effective temperature (K)	Phase angle <30° effective temperature (K)	Modified phase angle >40° effective temperature (K)
Aristarchus limb	N/A	4390 ± 660	1690 ± 130
Grimaldi limb	N/A	4560 ± 700	1710 ± 140
Langrenus limb	1750 ± 200	4740 ± 780	N/A
Cleomedes limb	1780 ± 180	3620 ± 580	N/A
Average	1770 ± 190	4330 ± 680	1700 ± 140

Additionally, a small subset of data were collected with a 1- and 2-arc min FOV (~112 and 224 km, respectively), and such data are contrasted to our 3-arc min data in Figure 7. While these data are within the range of 3-arc min results, they are systematically cooler. The smaller FOV measures relatively more atoms closer to the surface than the larger FOV and thus potentially a cooler velocity distribution. However, the overall systematic trends as a function of phase remains the same regardless of FOV size. Figure 8 shows temperature results dissected by month, with observations in December, January, and May having the highest temperatures during magnetotail passages. Finally, the measured radial velocity data, corrected for the Earth-Moon motion, of observations just off the limb are shown in Figure 9. A clear asymmetry between waxing and waning phase data is apparent in terms of Doppler shift.

Relative intensity as a function of phase for all equatorial data (limb only) are shown in Figure 10. Our relative intensities show large variability during magnetotail passage (0–30°) with a general trend of relative intensities increasing from full Moon to near quarter phases. The spectral fit uncertainties for waning phase observations are smaller than those of the waxing phase due to a reduction in scattered light off the selenographic west limb of the Moon (observations offset near Grimaldi and Aristarchus) which has a lower albedo due to the larger area of the surface covered by darker lunar maria.

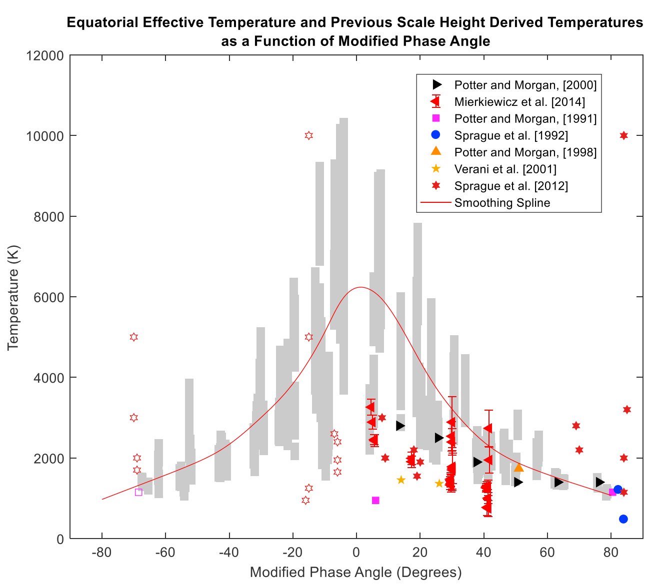

Figure 5. Scale height derived temperature data compiled by Sarantos et al. (2010); data from Sprague et al. (2012) and the line width derived temperature data of Mierkiewicz et al. (2014) are also included. The data range (including error bars) for our equatorial data is plotted in gray along with the smoothing spline of Figure 4. The waxing and waning phase derived temperatures of Potter et al. (2000) and the waning phase temperatures of Mierkiewicz et al. (2014) agree with the lower range of our data set.

4. Discussion

4.1. Implications of Line Width Measurements

The earlier line width derived temperatures by Mierkiewicz et al. (2014) ranged from 3260 ± 190 K near full Moon to 1000 ± 140 K at a phase angle of 42°; Potter et al. (2000) derived a temperature of 2900 K near full phase (4.3°), decreasing to 1400 K at phase angles of 50°–76°. Our line width derived temperatures range from 2500 to 9000 K during magnetotail passage, and while the lower range of these temperatures are in agreement with Mierkiewicz et al. (2014) and Potter et al. (2000) data, the upper range of these temperatures are higher overall by about a factor of 2–3 compared to both Mierkiewicz et al. (2014) data and previous scale height measurements (refer to Figure 5).

Previous ground-based observations, shown in Figure 5, and results presented here are higher than that expected for sodium atoms thermalized to the lunar surface, ~400 K at subsolar point (Stern, 1999), indicating that the source of these sodium atoms is dominated by an energetic, nonthermal process. One such process is PSD, which has an expected temperature of ~1200 K (Yakshinskiy & Madey, 1999). Although our temperatures at large phase angles (greater than 40°) are close to that of a PSD source (~1700 K), PSD itself does not sufficiently account for most of our temperatures, specifically near full Moon period. Even though PSD is a nonthermal source (Yakshinskiy & Madey, 1999, 2004; Schmidt, 2013), we see no evidence of a high-energy wing associated with non-Maxwellian profiles in our data.

One possible explanation for the difference in our line width derived effective temperatures compared to earlier work could be, in part, due to solar

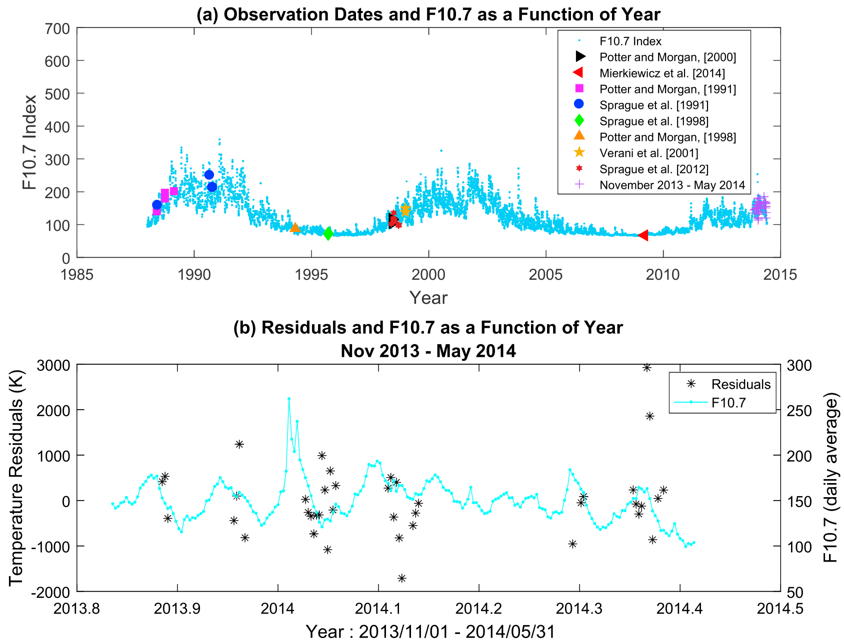

Figure 6. (a) Temperature data of Figure 5 and solar cycle as indicated by $F_{10.7}$ flux. (b) Temperature residuals as a function of $F_{10.7}$ daily averages. Residuals were obtained from subtracting a smoothing spline from temperature data averaged by day.

cycle effects. As seen in Figure 6a, the data of Potter and Morgan (1991) and Sprague et al. (1992) were collected close to solar maximum (cycle 22), whereas that of Sprague et al. (1998) and Potter and Morgan (1998) were collected close to solar minimum (also cycle 22). Data from Verani et al. (2001), Potter et al. (2000), and Sprague et al. (2012) were collected early in solar cycle 23, with the solar maximum in 2001. Using the same FPS instrument, the data from Mierkiewicz et al. (2014) were collected during solar minimum (cycle 24) while the data presented here were collected during solar maximum (cycle 24). We investigated the correlation to the solar $F_{10.7}$ flux by detrending our 2013–2014 data and plotting the residuals alongside $F_{10.7}$ flux daily averages (see Figure 6b). The detrending was done by binning data by day then fitting a smoothing spline to obtain residuals. We do not find an obvious correlation to small variations in solar output within this November 2013 to May 2014 period, although correlations to larger variations over a solar cycle remain possible. There is not enough data in 2009 (from Mierkiewicz et al., 2014) to determine a proper trend for the residual correlation with $F_{10.7}$ flux. Since data were limited in 2009, we combined 2009 data with the 2013–2014 data and repeated the detrending procedure, but no correlation was found. We have a large baseline of data extending from 2011 to 2017 with good phase coverage, and we will do a long-term correlation with solar flux in future work. Similarly, a more involved correlation of this data set to the Acceleration, Reconnection, Turbulence and Electrodynamics of the Moon's Interaction with the Sun proton and alpha/proton data will be done in a future work. However, for this 6-month period, this study on the $F_{10.7}$ flux remains inconclusive.

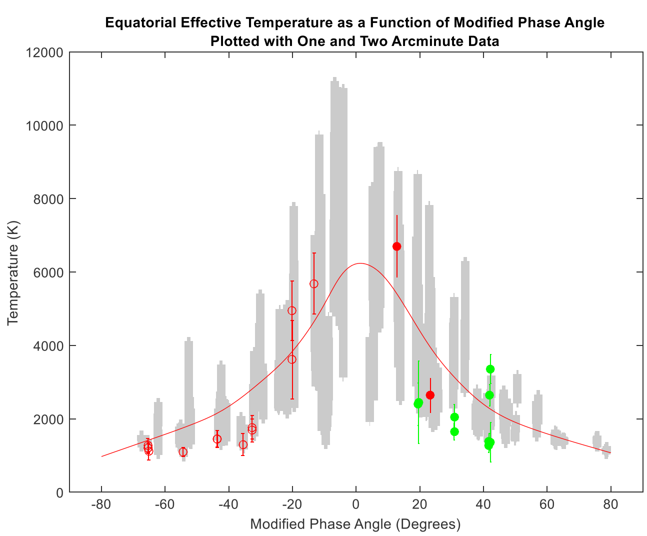

Figure 7. Gray error bars and the smoothing spline of Figure 4 plotted along with 1- (green) and 2- (red) arc min field-of-view data points. Open symbols represent waxing data, while filled symbols represent waning data.

Our measured radial velocities at the limb (Figure 9) show that waxing phase data are overall more redshifted than waning phase data and reach a maximum redshift right before full Moon. Waning phase data show a larger scatter compared to waxing phase data. The Doppler velocities provide an important and previously unavailable constraint on velocity distribution functions, and the asymmetry in the Doppler shift between waxing (dusk) and waning (dawn) phases might indicate a nonuniform

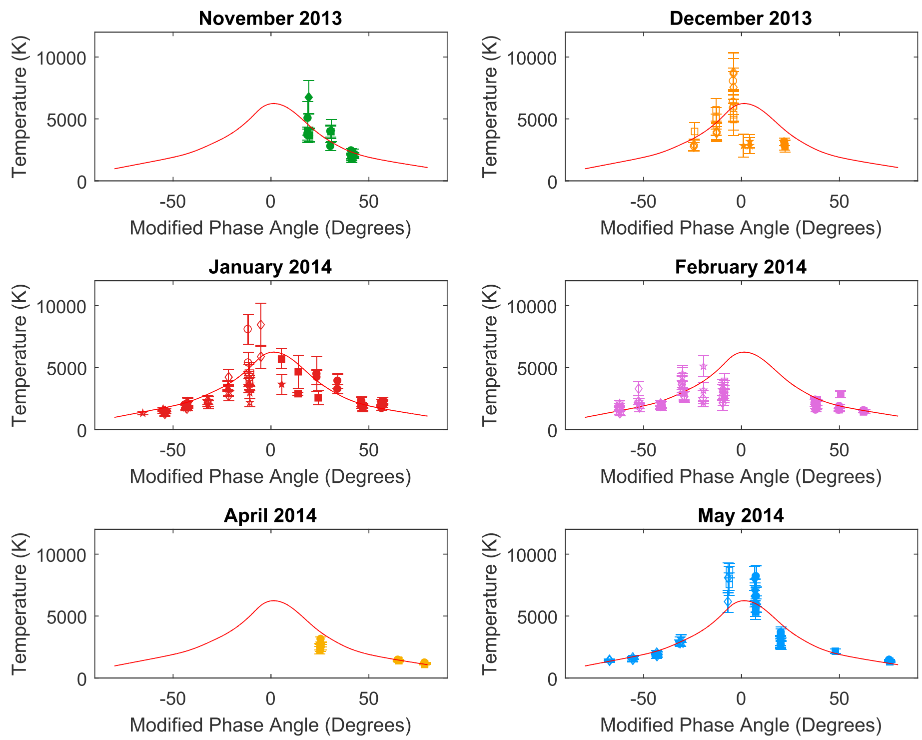

Figure 8. Equatorial temperature as a function of phase for each month. The largest magnetotail passage temperatures are seen in December, January, and May. The legend used in Figure 4 can be used for Figure 8.

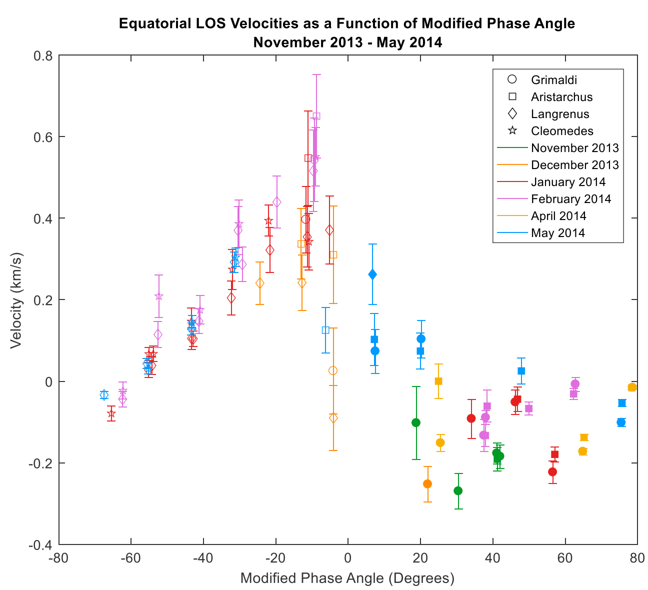

Figure 9. Sodium velocities in the lunar reference frame for data taken at the limb. Line of sight (LOS) velocities were corrected by using the self-reversal feature in the sodium calibration lamp to determine the rest wavelength of sodium and then correcting for Earth-Moon motion. The maximum redshift of approximately 0.6 km/s occurs right before full Moon. The general trend suggests that there is a linear increase in velocities for the waxing phase data toward full Moon and then rapidly decreasing after full Moon with more scatter in the waning phase data.

source distribution. For instance, a density asymmetry between dusk and dawn was measured by Kaguya data and indicated that sodium and potassium peak ion fluxes showed a 10° shift toward dawn (Yokota et al., 2014).

Relative intensity as a function of phase for data taken at the limb is shown in Figure 10 and is discussed in relation to LADEE UVS results in section 4.2. Relative intensity as a function of altitude for three data sets with good altitude coverage on 13 May 2014 off the Cleomedes Limb, 15 May 2014 off the Langrenus Limb, and 20 April 2014 off the Aristarchus Limb are shown in Figures 11a–11c, respectively. These data sets were used to calculate an apparent scale height using the methodology found in Sprague et al. (1992, equation A2) which is based on the Chamberlain and Hunten (1987) model. The apparent scale heights, corresponding Chamberlain temperatures, and the average line width derived temperature for a data set, are given in Table 3. Our empirically determined scale height temperatures vary by a factor of 1.2 (Figures 11a and 11b) to 3 (Figure 11c) from the average line width derived temperature. The differences between our scale height derived temperatures and line width derived effective temperatures indicate that methodology may play a role in explaining the difference between our data and previous scale height measurements. Our measurements are a direct probe of the line-of-sight (LOS) velocity of the gas at a given altitude while a scale height obtains a single temperature obtained from various altitudes along a slit. Previous ground-based measurements produced scale heights on the order of ~120 km for sodium (Potter & Morgan, 1988a; Sprague et al., 2012) on the lower end, and up to ~ 600 km (Sprague et al., 2012) on the higher end. A two-component model was used by both Potter and Morgan (1988a) and

10.1029/2018JE005717

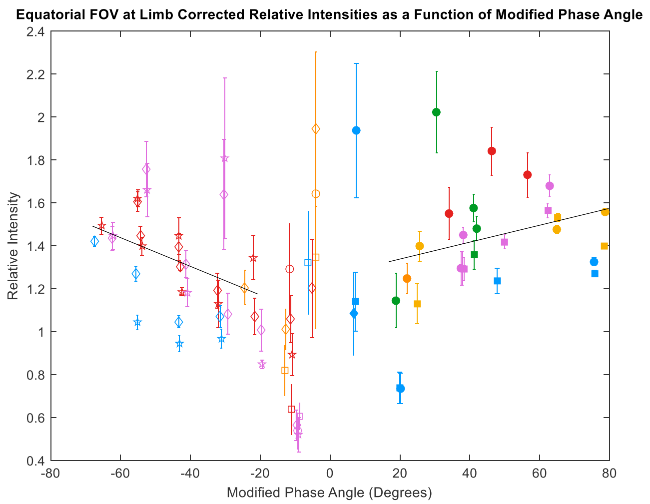

Figure 10. Relative intensity for limb equatorial data as a function of phase angle. Relative intensities have been divided by 1,000. The legend used in Figure 9 can be used here. Black lines highlighting the trends in intensity values between phase angles 20° and 80° for waxing and waning data are overplotted. While the month-to-month relative intensity remains around a value of 1.4, May 2014 is relatively flat compared to the other months. The overall pattern that is consistent is the relative intensities increase from full Moon toward quarter phases, with waning phase intensities being about 10% higher than waxing phase intensities.

Sprague et al. (2012) to explain the hot and cold components of the lunar exosphere. Our observations sample sodium atoms with varying velocity distributions but are more sensitive to the nonthermal or hot component due to our large FOV. These hot component velocity distributions could be due to sputtering, a nonthermal PSD population, or impact vaporization.

Our temperatures increase toward full Moon, with a range of 2500–9000 K during magnetotail passages. A fraction of this temperature increase may be the result of viewing geometry as the observational LOS intersects the extended lunar sodium tail for observations off the lunar limb at the time of full Moon. In this viewing geometry, sodium atoms with larger red shifts (as they move *downwind* of the Moon) will be observed, thereby widening the overall line profile and increasing the effective temperature (refer to sections 4.1.1 and 4.1.2). Although this redshifted Doppler component is expected to distort the observed profile near the red wing of the line, no such asymmetry has been detected (see Figures 2a and 2b). However, the increase in continuum levels due to scattered moonlight near full Moon does make detection of a red wing more problematic.

4.1.1. Geometrical Effects

To estimate the increase in line width due to viewing geometry/geometrical effects, a series of s-resolved sodium doublet synthetic emission spectra with equal intensities but shifted radial velocities (Figure 12) were coadded and fit. The s-resolved doublet is separated by 0.0198 Å (1.008 km/s) in a 3:5 intensity ratio. The width of each doublet

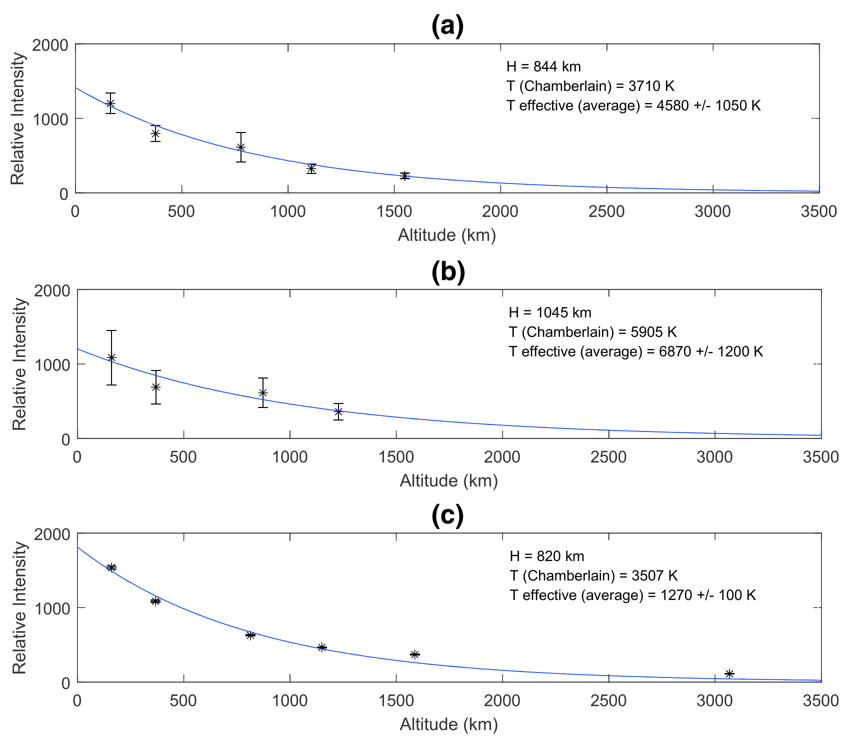

Figure 11. Relative intensity as a function of altitude for observations taken off the (a) Cleomedes limb on 13 May 2014 (phase ~ 18°), (b) Langrenus limb on 15 May 2014 (phase ~ 7°), and (c) Aristarchus limb on 20 April 2014 (phase ~ 65°). These data sets contain altitudes not included in the temperature analysis presented in this paper in order to effectively obtain scale height. The three nights used here sample latitudes from approximately −9°N to 24°N as the field of view is moved away from the Moon. The method in Sprague et al. (1992) was used to calculate the apparent scale height and scale height derived temperature. Note that the form of the exponential fit in blue is $y = a * \exp * (-b * x)$, where the scale height is found by taking the reciprocal of b.

Table 3
Apparent Scale Heights, Corresponding Chamberlain Temperatures, and Line Width Derived Temperatures

Figure	Date	Limb	Phase (degrees)	Apparent scale height (km)	Chamberlain temperature (K)	Line width derived temperature (K)
11a	13 May	Cleomedes	18	844	3710	4580 ± 1050
11b	15 May	Langrenus	7	1,045	5905	6870 ± 1200
11c	20 April	Aristarchus	65	820	3507	1270 ± 100

component is 1.73 km/s corresponding to a temperature of 1500 K. The model spectra are a sum of Doppler shifted spectra where each new sodium emission region is shifted by 0.15 km/s (half a spectral bin). The final model spectra has nine coadded spectra from 0 to 1.2 km/s to match the maximum velocity shift of 0.6 km/s as seen in our at-limb velocity data (refer to Figure 9). The model spectra are convolved with an IP and fit to determine the increase in line width due to the sum of different radial velocities. The results of these coadded synthetic spectra show an increase in line width of up to 0.3 km/s—an increase that does not adequately represent the increase in line width as we move toward smaller phase angles. While it is unrealistic to expect each contributing velocity component to have equal weight, we conclude that the bulk of the measured increase seen at small phase angles is not due to geometrical effects of *looking down the tail* (e.g., Line et al., 2012); rather it represents a genuine increase in scale height owing to higher-velocity sodium atoms.

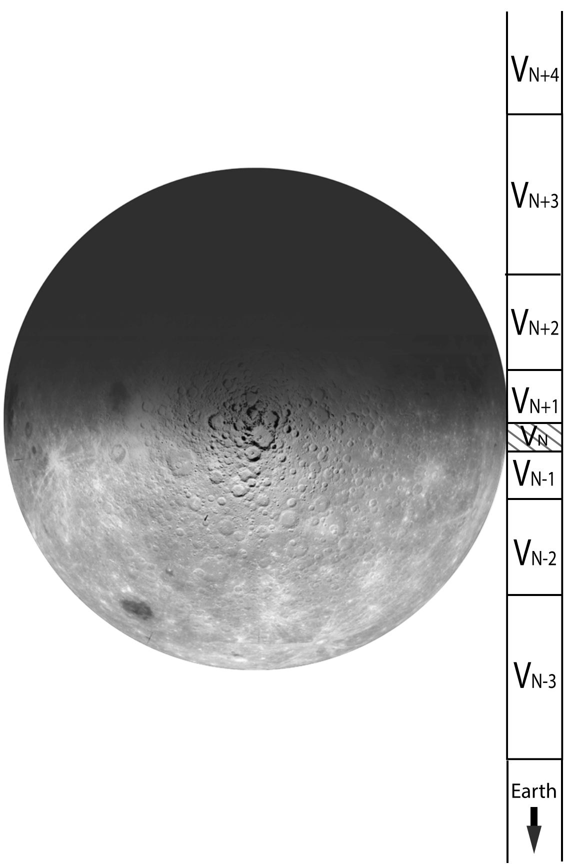

Figure 12. A schematic view of the field of view, during full Moon, as viewed from above the lunar north pole. For purposes of this model calculation the line of sight is divided in sections of equal column density and temperature (i.e., equal contributions to the sodium emission line profile) but with different radial velocities. The line-of-sight length for each section is arbitrary, but adjacent sections have a velocity difference of 0.15 km/s. For a total velocity range of 0–1.2 km/s or nine sections, the increase in line profile is 0.3 km/s.

4.1.2. Modeled Line Width and Center With a Particle Transport Model of Sodium Atoms

A complementary way to assess the effect of viewing geometry (Section 4.1.1) is to use a model of exospheric particle transport. Here the sodium transport model of Sarantos et al. (2010) was used to simulate velocity distributions of sodium atoms and to illustrate trends as a function of lunar phase angle. The version of the model used here accounts for the evolution of the velocity distribution of exospheric ejecta with altitude and the effects of gravity based on the distance of the neutrals from the Moon (Hartle, 1971) but does not account for radiation pressure and should only be considered as an initial step toward an interpretation. This model assumes a sticking coefficient of 1, that is, that sodium atoms efficiently lose their energy upon contact with the surface and come to a full stop after one bounce. Initial model runs consisted of a symmetric atmosphere with the source function centered at the subsolar point and having a cosine dependence with SZA. The velocity distribution functions of atoms leaving the surface were assumed to be Maxwellians, with different source temperatures (1500, 3000, 5000, and 10,000 K). For each source, the distribution of LOS velocities as a function of the velocity toward the Sun-Moon direction—which controls the *g* value (Killen et al., 2009)—was computed for different look directions of an Earth observer (lunar phase angles) by backtracking particles within three lunar radii of the tangent point, which was considered to lie at an altitude of 100 km.

The modeled line width as obtained from the model velocity distribution function, shown in Figure 13, indicates that the measured line width for the same source process should increase from quarter Moon (subsolar points) to full Moon (terminator side) since only the hottest particles with the largest ballistic range can travel from subsolar latitudes to the terminator/limb. This may explain the increase in line widths we see as we move to smaller phase angles. The increase in line width is expected to be fractional at small temperatures (~25% for an initial distribution of T = 3000 K from the lunar surface), but the line width almost doubles for T = 10,000 K (a proxy for sputtering). For hot source temperatures, the measurements should retrieve different widths for different months, particularly in waning phases, due to increased light scattering values of

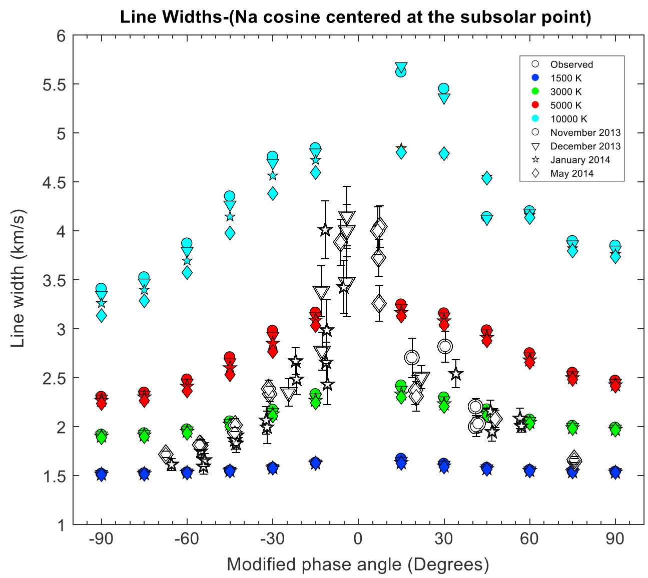

Figure 13. Sample symmetric exosphere model runs for a source with T = 1500, 3000, 5000, and 10000 K to assess geometric effects, for line width as a function of modified phase angle. No simulations were performed between −10° and 10° of lunar phase.

particles moving toward the Sun as the Moon-Sun velocity changes, an effect which was quantified using Jet Propulsion Laboratory ephemeris data for November, December, and May 2014. This effect is negligible for lower source velocities because an insignificant difference between particles that head toward and away from the Sun is found if escape rates are small. Line widths on the order of 3 km/s are expected when a source with an impact-like temperature (5000 K) is considered or more if sputtering is considered. This increase in line width for a 3000- and 5000-K source is approximately 0.5 and 0.8 km/s, respectively (Figure 13) and is larger than the ≲0.3 km/s increase in line width estimated from the possible velocity dispersion along the LOS in section 4.1.1 (Figure 12). These two different approaches indicate that the observed increase in line width at decreasing phase angle is not only due to changes in viewing geometry but rather signifies a changing relative importance of the considered source processes during a lunation.

Model Doppler shifts (Figure 14) approximately reproduce our at-limb velocity data (see Figure 9) when sources with Maxwellian ejection speed distributions with temperatures up to 5000 K are used, whereas sputtering by itself (10, 000 K) would produce excessive motion toward the observer. These simulations suggest that sodium atoms from a combination of PSD, impact vaporization, and sputtering sources are consistent with the trends reported in our measurements. The qualitative agreement between this initial model and our data provides additional confidence in our data acquisition and reduction methods.

4.2. Limb Relative Intensity Data and LADEE UVS Results

During its orbit around Earth, the Moon encounters three plasma environments: the magnetosphere, magnetosheath, and solar wind. The approximate locations of the boundaries that separate these three regions are at 30° and 70° phase angles (Sarantos et al., 2010). Near full Moon the Moon usually resides in the cooler and more rarified plasma of the lobes but briefly encounters hotter and denser plasma during plasma-sheet crossings. These crossings may temporarily augment the exosphere via ion sputtering, electron-stimulated desorption or other plasma impact effects (Wilson et al., 2006) and may explain the large variability in intensity and line width seen at small phase angles. Previous work by Potter et al. (2000) and Wurz et al. (2007) suggested that ion sputtering is an inefficient source mechanism for maintaining the lunar sodium exosphere, but the indirect effects of ions such as ion-enhanced diffusion might enhance the sodium reservoir and influence the exosphere. Therefore, depending on which region the Moon encounters, sodium exospheric abundances may vary. Sarantos et al. (2010) suggested that the plasma sheet ions may enhance the efficiency of PSD up to 2 times more than solar wind ions. The higher-energy plasma sheet ions can also penetrate further and potentially liberate sodium atoms that are buried deeper in the lunar soil.

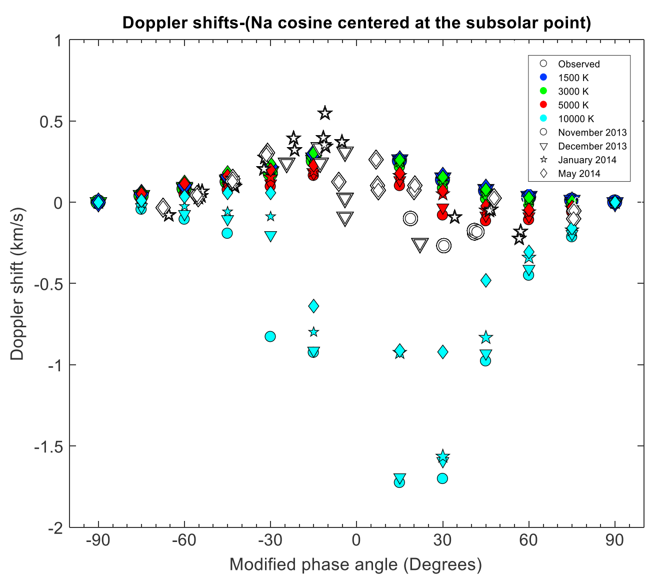

Figure 14. Sample symmetric exosphere model runs for Doppler shifts as a function of modified phase angle. No simulations were performed between −10° and 10° of lunar phase.

Due to observation geometries from Earth, sodium intensities from a time-invariant exosphere are expected to peak at quarter phases (Mendillo et al., 1997; Sarantos et al., 2010). This is because at quarter phases, limb observations probe subsolar points, where sodium abundances are presumed to peak (Mendillo et al., 1993; Potter & Morgan, 1998; Sprague et al., 1992). Our relative intensities increase going toward subsolar points from full Moon, with waning phase intensities being ~10% higher than waxing phase intensities.

LADEE measurements, however, indicated a sodium cycle during each lunation. LADEE UVS demonstrated a minimum sodium content a little after new Moon and a more complex trend around full Moon. That is, as the Moon passes into Earth's magnetotail the sodium column densities first slightly decreased and then increased significantly (i.e., by about a factor of 2) through full Moon reaching a maximum at ~30° phase angle, after which it begins to decrease again (Colaprete et al., 2016). Our observations probe different local times for different lunar phases and hence likely convolve spatial and temporal variations in sodium rate, whereas the LADEE UVS results of Colaprete et al. (2016) were made at around local noon and are a consistent representation of the temporal variability of the total content of the lunar exosphere.

Both our brightness trend and LADEE UVS observations can partly be explained by the lack of sputtering by the solar wind during magnetotail passage, although a higher sodium content on the lunar nearside (Athiray et al., 2014) can also explain these trends. Colaprete et al. (2016) noted that the absence of sputtering in the magnetotail should allow for sodium surface reservoirs to increase if ion-enhanced diffusion is an insignificant source of sodium. Once the Moon exits the magnetotail, solar wind sputtering resumes expelling adsorbed particles and thus the exospheric sodium decreases. In this interpretation, the solar wind is mainly a sink for exospheric adsorbates, unlike the suggestions of Potter et al. (2000) and Sarantos et al. (2010), and the monthly cycle evidenced by LADEE (and also surmised by Sarantos et al., 2010 and Sprague et al., 2012) must be attributed to nonuniform surficial sodium content.

Our lunar limb (relative) intensity data (Figure 10), corrected for Moon-Sun radial velocity shifts, show that overall relative intensities increase from full Moon toward quarter phases with some of the highest intensities recorded in December 2013, and May 2014 during magnetotail passage. Our Moon-Sun radial velocity shift correction adjusts for the varying solar flux seen by sodium emission atoms due to Doppler shift changes relative to the bottom of the Fraunhofer feature. Intensity values from Table 1 of Sarantos et al. (2010) show a general trend toward reduced exospheric sodium intensity going from a pure solar wind environment (region of high ion flux) to the magnetosphere (region of low ion flux). Our relative intensity data follow a similar trend, with intensities decreasing, going from phase angle 70° toward phase angle 0°. Our data, however, show a large variation in relative intensity within the magnetosphere region (phase angles less than 30°) including a few of the brightest intensity data. Hence, our data indicate that various plasma environments may influence the evolution of the exosphere.

5. Summary and Conclusions

This unique data set raises new questions and will provide additional insight into the spatial and temporal variation of the lunar sodium exosphere, especially with future work into possible correlations with Earth's magnetospheric plasma environment and solar wind conditions. Our relative intensity data show large variations when the Moon is located in the magnetosphere region (phase angles $<30°$) and also indicate that the various plasma regions the Moon encounters can influence the sodium exosphere.

Our line width and line width derived temperatures show a systematic increase from quarter Moon to full Moon. While temperatures at phase angles $>40°$ and larger are consistent with a PSD source (~1700 K), temperatures in the range of 2500–9000 K were routinely measured near Full Moon (0–30°). The upper range of our temperatures is overall higher than those of previous studies by about a factor of 2–3 near full Moon. This systematic trend could either arise from a single velocity distribution, perhaps nonthermal, that steepens due to geometrical effects as we look down the tail, or can indicate a transition from a PSD-dominated atmosphere to a mix of sources when we look near the terminator. Either way, the dominant cause of the upper range of our temperatures during magnetotail passage is not due to geometrical effects as we have shown that the bulk of the measured increase in line width from near quarter phase to small phase angles exceeds the geometrical effects of looking *down the tail*. Particle simulations confirm that line width from a single source increases when phase angles decrease as low energy atoms map along subsolar points during quarter phases and high-energy atoms map along terminator lines during full Moon. However, no source could reproduce temperature results for all phases. Line widths of ~3 km/s are expected when an impact source of 5000 K is considered and higher if sputtering is an important source. From these two lines of evidence we believe that impact vaporization, sputtering, and/or a non-thermal distribution for PSD likely combine to produce the trends shown here. In conclusion, although the systematic trend can be explained, the magnitude of the line width increase near full Moon is puzzling and requires additional modeling (see Sarantos et al., 2017) to extract the speed distribution with which sodium atoms are ejected from the surface.

As to the cause of the observed short and long-term temperature deviations from this systematic trend, possible reasons include a solar cycle variation, meteor showers, and solar wind variations. No correlation between $F_{10.7}$ and this data set were found. Data collected with the same instrument during March 2009 by Mierkiewicz et al. (2014; solar minimum) show similar trends with lunar phase but lower temperatures by about a factor of 2–3 near full Moon than the upper range of data presented here, which were collected during solar maximum. Long-term solar cycle effects will, however, be addressed in a future work in which data obtained between 2011 and 2017 will be analyzed. Some other possibilities that could generate large temperatures like those seen in our data include a nonthermal PSD population, micrometeoroid impact vaporizations, and sputtering sources. The only major meteor shower that had its peak coincide with our observations were the Geminids (13/14 December), but we do not see any distinct responses in the sodium exosphere in terms of increased temperatures for that event, although we only obtained measurements 1 day after the peak of the Geminids. Sputtering by charged particles from different plasma environments (e.g., plasma sheet vs. lobes, variability in magnetosheath, and solar wind) can produce variable temperatures depending on the energy and flux of particles in each environment, which affect the sputtering contributions to the exosphere relative to the other sources. Analysis of the in situ plasma environment measurements obtained by the Acceleration, Reconnection, Turbulence and Electrodynamics of the Moon's Interaction with the Sun mission will help further detangle the roles played by these suggested source mechanisms.

Acknowledgments
The authors thank the National Solar Observatory at Kitt Peak for use of their fine telescope and extend special thanks to Detrick Branston, Matt Penn, and the Kitt Peak mountain staff. We thank ERAU students Maurice Wilson, Robert Kallio, and Andrea Hughes who helped with our observing runs and the University of Maryland student Edward Williams for helping retrieve and plot the output of particle simulations. We also are appreciative of the advice from Jody Wilson, University of New Hampshire. We also thank Michael Line, Arizona State University, for his observing support and model/data discussions. The authors also thank the reviewers for their thorough review and excellent suggestions. This work was supported by NASA grants NNX11AE38G and NNX13AL30G and by the Solar System Exploration Research Virtual Institute (SSERVI). All line width, phase, temperature, and intensity data used in this work can be found in Table S1 of the supporting information.

References

Athiray, P. S., Narendranath, S., Sreekumar, P., & Grande, M. (2014). C1XS results—First measurement of enhanced sodium on the lunar surface. *Planetary and Space Science*, *104*, 279–287. https://doi.org/10.1016/j.pss.2014.10.010

Chamberlain, J. W., & Hunten, D. M. (1987). *Theory of planetary atmospheres*. Orlando: Academic Press.

Coakley, M. M., Roesler, F. L., Reynolds, R. J., & Nossal, S. (1996). Fabry-Perot CCD annular-summing spectroscopy: Study and implementation for aeronomy applications. *Applied Optics*, *35*(33), 6479–6493. https://doi.org/10.1364/AO.35.006479

Colaprete, A., Sarantos, M., Wooden, D. H., Stubbs, T. J., Cook, A. M., & Shirley, M. (2016). How surface composition and meteoroid impacts mediate sodium and potassium in the lunar exosphere. *Science*, *351*(6270), 249–252. https://doi.org/10.1126/science.aad2380

Domingue, D. L., Patrick, L. K., Killen, R. M., Sprague, A. L., Sarantos, M., Cheng, A. F., et al. (2007). Mercury's atmosphere: A surface-bounded exosphere. *Space Science Reviews*, *131*(1-4), 161–186. https://doi.org/10.1007/s11214-007-9260-9

Halekas, J. S., Benna, M., Mahaffy, P. R., Elphic, R. C., Poppe, A. R., & Delory, G. T. (2015). Detections of lunar exospheric ions by the LADEE Neutral Mass Spectrometer. *Geophysical Research Letters*, *42*, 5162–5169. https://doi.org/10.1002/2015GL064746

Hartle, R. E. (1971). Model for rotating and nonuniform planetary exospheres. *The Physics of Fluids*, *14*(12), 2592–2598. https://doi.org/10.1063/1.1693379

Horányi, M., Szalay, J. R., Kempf, S., Schmidt, J., Grün, E., Srama, R., & Sternovsky, Z. (2015). A permanent, asymmetric dust cloud around the Moon. *Nature*, *522*(7556), 324–326. https://doi.org/10.1038/nature14479

Ip, W. H. (1991). The atomic sodium exosphere/coma of the Moon. *Geophysical Research Letters*, *18*, 2093–2096. https://doi.org/10.1029/91GL02549

Janches, D., Pokorný, P., Sarantos, M., Szalay, J. R., Horányi, M., & Nesvorný, D. (2018). Constraining the ratio of micrometeoroids from short- and long-period comets at 1 AU from LADEE observations of the lunar dust cloud. *Geophysical Research Letters*, *45*, 1713–1722. https://doi.org/10.1002/2017GL076065

Kagitani, M., Taguchi, M., Yamazaki, A., Yoshikawa, I., Murakami, G., Yoshioka, K., et al. (2010). Variation in lunar sodium exosphere measured from lunar orbiter SELENE (Kaguya). *Planetary and Space Science*, *58*(12), 1660–1664. https://doi.org/10.1016/j.pss.2010.07.025

Killen, R., Shemansky, D., & Mouawad, N. (2009). Expected emission from Mercury's exospheric species, and their ultraviolet-visible signatures. *The Astrophysical Journal Supplement Series*, *181*(2), 351–359. https://doi.org/10.1088/0067-0049/181/2/351

Line, M. R., Mierkiewicz, E. J., Oliversen, R. J., Wilson, J. K., Haffner, L. M., & Roesler, F. L. (2012). Sodium atoms in the lunar exotail: Observed velocity and spatial distributions. *Icarus*, *219*, 609–617.

Madey, T. E., Yakshinskiy, B. V., Ageev, V. N., & Johnson, R. E. (1998). Desorption of alkali atoms and ions from oxide surfaces—Relevance to origins of Na and K in atmospheres of Mercury and the Moon. *Journal of Geophysical Research*, *103*, 5873–5887. https://doi.org/10.1029/98JE00230

McNutt, D. P., & Mack, J. E. (1963). Telluric absorption, residual intensities, and shifts in the Fraunhofer D lines. *Journal of Geophysical Research*, *68*, 3419–3429. https://doi.org/10.1029/JZ068i011p03419

Mendillo, M., Emery, J., & Flynn, B. (1997). Modeling the Moon's extended sodium cloud as a tool for investigating sources of transient atmospheres. *Advances in Space Research*, *19*(10), 1577–1586. https://doi.org/10.1016/S0273-1177(97)00371-2

Mendillo, M., Flynn, B., & Baumgardner, J. (1993). Imaging experiments to detect an extended sodium atmosphere on the Moon. *Advances in Space Research*, *13*(10), 313–319. https://doi.org/10.1016/0273-1177(93)90085-P

Mierkiewicz, J., Oliversen, R. J., Roesler, F. L., & Lupie, O. L. (2014). High-resolution spectroscopy of the lunar sodium exosphere. *Journal of Geophysical Research: Space Physics*, *119*, 4950–4956. https://doi.org/10.1002/2014JA019801

Morgan, T. H., & Shemansky, D. E. (1991). Limits to the lunar atmosphere. *Journal of Geophysical Research*, *96*, 1351–1367. https://doi.org/10.1029/90JA02127

Potter, A. E., Killen, R. M., & Morgan, T. H. (2000). Variation of the lunar sodium during passage of the Moon through the Earth's magnetotail. *Journal of Geophysical Research*, *105*, 15,073–15,084. https://doi.org/10.1029/1999JE001213

Potter, A. E., Mendell, W., & Morgan, T. H. (1984). Lunar luminescence and the filling-in of the Fraunhofer lines in moonlight. *Journal of Geophysical Research*, *89*, C240–C244. https://doi.org/10.1029/JB089iS01p0C240

Potter, A. E., & Morgan, T. H. (1988a). Discovery of sodium and potassium vapor in the atmosphere of the Moon. *Science*, *241*(4866), 675–680. https://doi.org/10.1126/science.241.4866.675

Potter, A. E., & Morgan, T. H. (1988b). Extended sodium exosphere of the Moon. *Geophysical Research Letters*, *15*, 1515–1518. https://doi.org/10.1029/GL015i013p01515

Potter, A. E., & Morgan, T. H. (1991). Observations of the lunar sodium exosphere. *Journal of Geophysical Research*, *18*, 2089–2092. https://doi.org/10.1029/91GL02621

Potter, A. E., & Morgan, T. H. (1994). Variation of lunar sodium emission intensity with phase angle. *Journal of Geophysical Research*, *21*, 2263–2266. https://doi.org/10.1029/94GL01702

Potter, A. E., & Morgan, T. H. (1998). Coronagraphic observations of the lunar sodium exosphere near the lunar surface. *Journal of Geophysical Research*, *103*, 8581–8586. https://doi.org/10.1029/98JE00059

Sarantos, M., Killen, R. M., Surjalal, S. A., & Slavin, J. A. (2008). Influence of plasma ions on source rates for the lunar exosphere during passage through the Earth's magnetosphere. *Geophysical Research Letters*, *35*, L04105. https://doi.org/10.1029/2007GL032310

Sarantos, M., Killen, R. M., Surjalal, S. A., & Slavin, J. A. (2010). Sources of sodium in the lunar exosphere: Modeling using ground-based observations of sodium emission and spacecraft data of the plasma. *Icarus*, *205*(2), 364–374. https://doi.org/10.1016/j.icarus.2009.07.039

Sarantos, M., Kuruppuaratchi, D. C. P., Pokorny, P., Robertson, S. D., Williams, E., Oliversen, R. J., et al. (2017). Improved velocity distributions for exospheric Na and K surrounding the Moon, AGU Fall Meeting Abstracts.

Schmidt, C. A. (2013). Monte Carlo modeling of north-south asymmetries in Mercury's sodium exosphere. *Journal of Geophysical Research: Space Physics*, *118*, 4564–4571. https://doi.org/10.1002/jgra.50396

Smith, S., Wilson, J., Baumgardner, J., & Mendillo, M. (1999). Discovery of the distant lunar sodium tail and its enhancement following the Leonid meteor shower of 1998. *Geophysical Research Letters*, *26*, 1649–1652. https://doi.org/10.1029/1999GL900314

Smyth, W. H., & Marconi, M. L. (1995). Theoretical overview and modeling of the sodium and potassium atmospheres of the Moon. *The Astrophysical Journal*, *443*, 371–392. https://doi.org/10.1086/175532

Sprague, A. L., Hunten, D. M., Kozlowski, R. W. H., Grosse, F. A., Hill, R. E., & Morris, R. L. (1998). Observations of sodium in the lunar atmosphere during international lunar atmosphere week, 1995. *Icarus*, *131*(2), 372–381.

Sprague, A. L., Kozlowski, R. W. H., Hunten, D. M., Wells, W. K., & Grosse, F. A. (1992). The sodium and potassium atmosphere of the Moon and its interaction with the surface. *Icarus*, *96*(1), 27–42. https://doi.org/10.1016/0019-1035(92)90004-Q

Sprague, A. L., Sarantos, M., Hunten, D. M., Hill, R. E., & Kozlowski, R. W. H. (2012). The lunar sodium atmosphere: April–May1998. *Canadian Journal of Physics*, *90*(8), 725–732. https://doi.org/10.1139/p2012-072

Stern, S. A. (1999). The lunar atmosphere: History, status, current problems, and context. *Reviews of Geophysics*, *37*, 453–491. https://doi.org/10.1029/1999RG900005

Szalay, J. R., Horányi, M., Colaprete, A., & Sarantos, M. (2016). Meteoritic influence on sodium and potassium abundance in the lunar exosphere measured by LADEE. *Geophysical Research Letters*, *43*, 6096–6102. https://doi.org/10.1002/2016GL069541

Tenishev, V., Rubin, M., Tucker, O., Combi, R., & Sarantos, M. (2013). Kinetic modeling of sodium in the lunar exosphere. *Icarus*, *226*(2), 1538–1549. https://doi.org/10.1016/j.icarus.2013.08.021

Tyler, A. L., Hunten, D. M., & Kozlowski, R. (1988). Observations of sodium in the tenuous lunar atmosphere. *Geophysical Research Letters*, *15*, 1141–1144. https://doi.org/10.1029/GL015i010p01141

Verani, S., Barbieri, C., Benn, C., & Cremonese, G. (1998). Possible detection of meteor stream effects on the lunar sodium atmosphere. *Planetary and Space Science*, *46*, 1003–1006. https://doi.org/10.1016/S0032-0633(98)00024-5

Verani, S., Barbieri, C., Benn, C. R., Cremonese, G., & Mendillo, M. (2001). The 1999 quadrantids and the lunar Na atmosphere. *Monthly Notices of the Royal Astronomical Society*, *327*(1), 244–248. https://doi.org/10.1046/j.1365-8711.2001.04748.x

Wilson, J. K., Mendillo, M., & Spence, H. E. (2006). Magnetospheric influence on the Moon's exosphere. *Journal of Geophysical Research*, *111*, A07207. https://doi.org/10.1029/2005JA011364

Wurz, P., Rohner, U., Whitby, J. A., Kolb, C., Lammer, H., Dobnikar, P., & Martin-Fernändez, J. A. (2007). The lunar exosphere: The sputtering contribution. *Icarus*, *191*(2), 486–496. https://doi.org/10.1016/j.icarus.2007.04.034

Yakshinskiy, B. V., & Madey, T. E. (1999). Photon-stimulated desorption as a substantial source of sodium in the lunar atmosphere. *Nature*, *400*(6745), 642–644. https://doi.org/10.1038/23204

Yakshinskiy, B. V., & Madey, T. E. (2004). Photon-stimulated desorption of Na from a lunar sample: Temperature-dependent effects. *Icarus*, *168*, 53–59. https://doi.org/10.1016/j.icarus.2003.12.007

Yokota, S., Tanaka, T., Saito, Y., Asamura, K., Nishino, M. N., Fujimoto, M., et al. (2014). Structure of the ionized lunar sodium and potassium exosphere: Dawn-dusk asymmetry. *Journal of Geophysical Research: Planets*, *119*, 798–809. https://doi.org/10.1002/2013JE004529